RESEARCH ARTICLE

Exploring Charge Transport and Hysteresis Effects in Perovskite Solar Cells Through Dynamic Measurements and Analytical Modeling

Gabriel L. Nogueira[1] | Victor Lopez-Richard[2] | Luiz A. Meneghetti Jr.[2] | Fabian Hartmann[3] | Carlos F. O. Graeff[1]

[1]Department of Physics and Meteorology, School of Sciences, Sao Paulo State University (UNESP), Bauru, Sao Paulo, Brazil | [2]Department of Physics, Federal University of Sao Carlos (UFSCar), Sao Carlos, Sao Paulo, Brazil | [3]Julius-Maximilians-Universität Würzburg, Physikalisches Institut and Wüzburg-Dresden Cluster of Excellence ct.qmat, Lehrstuhl für Technische Physik, Würzburg, Deutchland

Correspondence: Gabriel L. Nogueira (leonardo.nogueira@unesp.br) | Carlos F. O. Graeff (carlos.graeff@unesp.br)

ABSTRACT

Perovskite solar cells (PSCs) have emerged as a promising photovoltaic technology, already achieving efficiencies surpassing 26%. However, effects such as hysteresis are commonly observed due to the interplay of ionic and electronic transport occurring over different timescales. In this work, we presented a unified analytical framework for characterizing charge transport and hysteresis in PSCs, validated through experiments on standard n-i-p mesoporous devices. Beyond small-signal impedance spectroscopy, our model also explains the large-signal response under pulsed and sinusoidal voltage inputs. Sinusoidal I–V analysis combined with the Fourier transform revealed the system's transition from capacitive to inductive-like response, depending on excitation frequency. Therefore, this work provides not only theoretical insights but also a step-by-step methodology. By combining small- and large-signal experiments within a single interpretive framework, our approach offers a physically grounded and experimentally accessible strategy for decoding and managing nonlinear and memory-driven effects in PSCs.

1 | Introduction

Metal halide perovskites have garnered significant attention for their potential in solar cell applications, driven by remarkable performance improvements in recent years. Perovskite solar cells (PSCs) have achieved power conversion efficiencies (PCEs) exceeding 26%, a milestone that, in combination with their ease of fabrication, has placed them at the forefront of emergent photovoltaic technologies [1]. Despite this impressive performance, perovskite-based photovoltaic devices face challenges related to stability and metastability, which complicate, for example, the accurate assessment of solar-to-electrical energy conversion efficiency [2]. A prominent issue is the hysteresis in the current–voltage curves, which

manifests as discrepancies between the forward and reverse voltage sweeps [3]. These effects have prompted extensive research into the fundamental properties of halide perovskites, intending to unlock their full potential for sustainable energy conversion.

These materials exhibit dual ionic-electronic transport. Typically, electronic responses occur within hundreds of nanoseconds, while the redistribution of mobile ions unfolds over seconds to minutes. Anta et al. [4] highlighted this interplay, showing how external stimuli influence ionic movement and how slow reorganization of ions can influence electronic transport. Tress et al., linked hysteresis in $CH_3NH_3PbI_3$ to ion diffusion and charge-carrier collection efficiency [5]. These dynamics are

regarded as a key factor underlying hysteresis in current–voltage (J–V) measurements [6]. The J–V characteristics of PSCs are sensitive to parameters such as voltage sweep rate, preconditioning protocols, and sweep direction. Techniques such as impedance spectroscopy (IS) have been instrumental in elucidating the interactions between ionic and electronic processes [7, 8]. Additionally, transport models, including atomistic simulations and drift-diffusion models, have furthered our understanding of these complex phenomena [4].

Recent studies draw parallels between PSCs and memristors, suggesting that the resistive switching response commonly observed in memristors may naturally occur in PSCs due to ionic-controlled interface recombination [9] and other transport mechanisms. This underscores the suitability of using memristor models in systems involving materials with mobile ions [6, 10, 11]. A memristor is a nonlinear electrical component whose resistance depends on the history of applied voltage and current, effectively 'remembering' past electrical states [12, 13]. In PSCs, the slow redistribution of ions under external stimuli leads to resistive switching effects, analogous to memristive devices [13–15]. The architecture of the PSC device has a strong effect on hysteresis. In planar PSCs, hysteresis is often attributed to inefficient charge transfer at the perovskite-transport layer interface, leading to charge trapping and recombination [16]. Mesoporous PSCs, while exhibiting improved charge extraction compared to planar architectures, often show more pronounced hysteresis than typically observed in p-i-n devices [17].

In this study, we present a unified framework that combines dynamic measurements with an analytical transport model to investigate charge transport and hysteresis phenomena in PSCs. Several recent efforts have advanced the understanding of these effects, particularly through the use of drift-diffusion simulations and generalized equivalent circuit models. For example, Clarke et al. [18] offer a comprehensive classification of impedance spectra in PSCs and demonstrate how effects such as inductive loops and multiple arcs can emerge from field screening, interface recombination, and ion migration. Although powerful, these numerical approaches can be computationally intensive and sensitive to the parameters used. In another important contribution, Álvarez et al. [19] proposed a consistent modeling scheme across modulated techniques such as IS, intensity-modulated photocurrent spectroscopy, and intensity-modulated photovoltage spectroscopy, using a harmonized equivalent circuit strategy to extract kinetic parameters from light and voltage perturbations. While these models have provided valuable insights, they often rely on fitted circuit elements whose physical interpretations are not always straightforward, particularly when addressing nonlinear or memory-rich responses. In contrast, our model is derived analytically from charge transport equations that incorporate memory processes with explicit voltage-dependent activation and relaxation times. This allows us to interpret complex responses, such as transient current growth, inductive-like low-frequency loops, and frequency-dependent phase lags, without resorting to arbitrary lumped elements. By combining small- and large-signal experiments (including IS, voltage transients, and sinusoidal excitation) within a single interpretive framework, we offer a physically consistent and experimentally accessible method that advances both the analysis and the understanding of hysteresis and dynamic transport in PSCs.

2 | Results and Discussion

2.1 | Hysteresis Observation in PSCs

The J–V curves were obtained by sweeping the applied voltage over a specific range. Figure 1a,b shows forward and reverse bias voltage scans from representative devices, in which hysteresis is clearly observed. The average device performance yielded a PCE of 15.1%, with J_{sc} = 22.9 mA cm^{-2}, V_{oc} = 0.97 V, and a fill factor of 67.5%, measured at a scan rate of 250 mV s^{-1} in reverse direction—values consistent with prior reports [20, 21]. The integrated current from external quantum efficiency (EQE) data achieved 21.5 mA cm^{-2}, and we extracted a photovoltaic bandgap of 1.65 eV (Figure S1a–c, Supporting Information). The observed counterclockwise hysteresis is classified as normal [22, 23] and becomes more pronounced at faster sweep rates. In the forward sweep direction, the effect of the scan rate on PCE is especially critical, as provided in Figure 1c,d. To provide a broader view of the device response, we have included additional data obtained using another equipment, which allows finer control over scan rate and pre-bias conditioning. Figure S2a, Supporting Information, highlights the preconditioning effect on the J–V curve. As shown in the inset of Figure S2a, Supporting Information, the device reaches a steady-state current after approximately 20 s. Figure S2b, Supporting Information, shows the hysteresis response for a larger variation in scan rates.

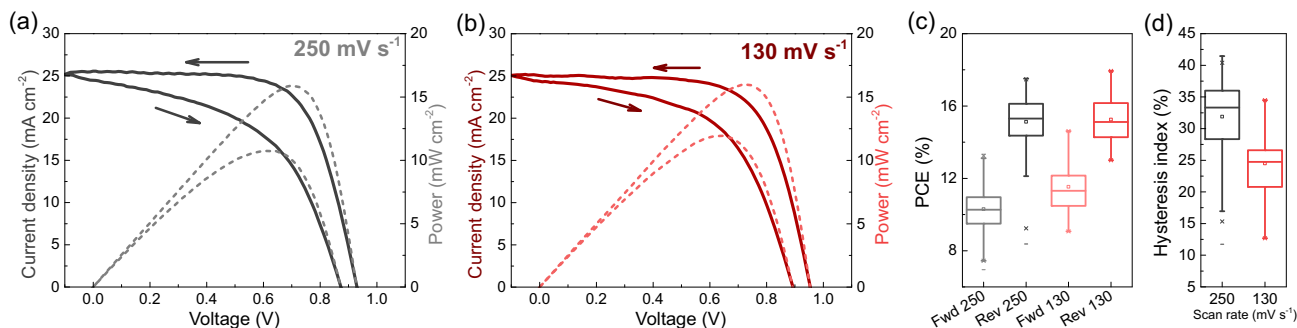**FIGURE 1** | Representative J–V curves of the PSCs under (a) 250 mV s^{-1} and (b) 130 mV s^{-1}. Box chart showing the dependence of (c) PCE and (d) hysteresis index on the scan rate. Data obtained under the solar simulator of 1 sun (AM 1.5 G).

These dynamics may be associated with recombination pathways [24], which we explored by the current–voltage characteristics under different illumination intensities (Figure S3a, Supporting Information). Evaluating the open-circuit voltage, V_{oc}, as a function of illumination intensity provides valuable insights into recombination kinetics in PSCs. An ideality factor of $n = 1$ suggests that second order (bimolecular) charge-carrier recombination dominates, whereas $n = 2$ corresponds to first order (monomolecular) trap-assisted nonradiative recombination. Our devices have an ideality factor of 1.65, aligning with our previous findings using a hysteresis-free device with an inverted architecture [25]. These results for mesoporous PSC suggest that trap-assisted monomolecular recombination dominates near the interfaces, since hysteresis can arise from the combined effect of mobile ions and recombination near the perovskite-contact interfaces [26]. Additional details about the ideality factor are provided in the Supplementary Information (SI).

While the slow ionic movement within the perovskite layer is widely recognized as a primary cause of the dynamic responses observed in PSCs [27], IS and equivalent circuit models alone are insufficient to identify the ionic species involved. Our results indicated that bulk ion migration cannot fully account for hysteresis; instead, interfacial processes, which involve the capture and release of localized charges, play a significant role [28]. After diffusion, accumulated ions modify interfacial barriers and impact charge extraction at contacts [29].

2.2 | Transient Response and AC Stimuli

Dynamic processes are critical for stabilizing PSCs, particularly under large excitation [6]. The sinusoidal stimulus is used for detailed frequency-dependent dynamics, analogous to but complementary to conventional IS. Despite the illumination effects discussed in the previous section, we focus here on dark conditions, where the inductive-like characteristic is observed. Additionally, in the absence of light, charge carriers are injected solely from the contacts, making the system less susceptible to photodegradation effects [30].

Figure 2 illustrates the current response to 1 s voltage pulses under different amplitudes in the dark. Under a 0.7 V pulse (Figure 2a), the device exhibits an initial microsecond-scale spike followed by a steady-state current. When the bias exceeds the built-in potential (V_{bi}), the current spike is followed by a gradual increase (Figure 2b). This so-called 'negative transient spike' is typically both voltage- and light-dependent (Figure 2c) [11, 31].

Figure 2d–f decompose the response to a 1.1 V pulse into three distinct timescales, corresponding to capacitive and 'inductive' responses, as commonly described in the literature [32]. The transient response comprises an initial fast spike, a subsequent current decay, and a slower current increase that stabilizes over time. The fastest process (1 µs), shown in Figure 2d, reflects a pure capacitive effect. This microsecond regime is analyzed through a simulation of the initial current spike obtained from the derivative of the applied voltage (dV/dt). The estimated capacitance of ≈18.5 nF is consistent with the value extracted via IS in the ≈10–100 kHz frequency range. In contrast, Figure 2e,f display the same current curve fitted with a triple-exponential

function, highlighting two distinct regimes: the subsequent current decay around 1 ms and the onset of slower current growth beyond 10 ms.

The current response was modeled using a sum of three exponential terms: $f(x) = A + b_1 \exp\left(-\frac{t}{\tau_1}\right) + b_2 \exp\left(-\frac{t}{\tau_2}\right) + b_3 \exp\left(-\frac{t}{\tau_3}\right)$. Although usually related to capacitive and inductive elements, we assume that the decay and growth exponents correspond to a competition of trapping rates and carrier generation, as described by Equation (5) [33]. A capacitance plot and a table summarizing the exponential parameters are provided in the SI. We highlight the third term, where the negative value of b_3 indicates that the carrier generation processes become predominant above the characteristic time (τ_3) of about 20 ms.

Fast dynamics, typically on timescales from 10^{-12} to 10^{-6} s, are attributed to electronic processes, while slower dynamics, lasting over 1 s, are associated with electrochemical or ionic processes [34]. The microsecond-scale capacitive response observed in our experiments (Figure 2d) may be linked to recombination processes either at the interfaces or within the perovskite bulk. While some uncertainty exists regarding the dynamics on the microsecond timescale, this primarily affects the interpretation of the capacitance associated with the fastest response. This microsecond-scale response observed in our experiments (Figure 2d) may be linked to recombination processes at the interfaces or within the perovskite bulk. As discussed in Section 3.1, an ideality factor of 1.65 suggests that, while trap-assisted recombination contributes to the overall response, it is not the dominant mechanism. However, it may also involve faster processes than those typically reported for perovskites. Importantly, this does not compromise the validity of the exponential fitting or the extracted time constants for the main processes, which remain consistent with the expected perovskite dynamics.

We infer that the slower processes, exceeding 1 s, are associated with ionic motion. This assignment is supported by comparing the timescale of the current decay in Figure 2e, 0.1–2 ms, with the negative susceptance below 1000 Hz in Figure 1g. The origin of these slow dynamics may involve relatively fast Li^+ ions from the spiro transport layer, slower movement of heavier ions between the perovskite and transport layers, or the formation of ion vacancies at grain boundaries in the perovskite film [35]. It is important to note that the presence of transients imposes additional challenges for spectral analysis, as highlighted by Lopez-Richard et al. [36].

It is important to stress that the growth or decay observed in a transient current response following a rectangular voltage pulse cannot be unambiguously attributed to the nature of the underlying physical process, such as carrier trapping or the activation of nonequilibrium transport processes, based solely on its shape [37, 38]. This is because the direction and amplitude of the transient response depend not only on the intrinsic characteristics of the process (e.g., relaxation time, nature of the trapping or activation mechanism), but also critically on the initial state of the system, which often remains unknown or uncontrolled. In systems with internal memory, like PSCs with mixed ionic-electronic conduction, the transient reflects the difference
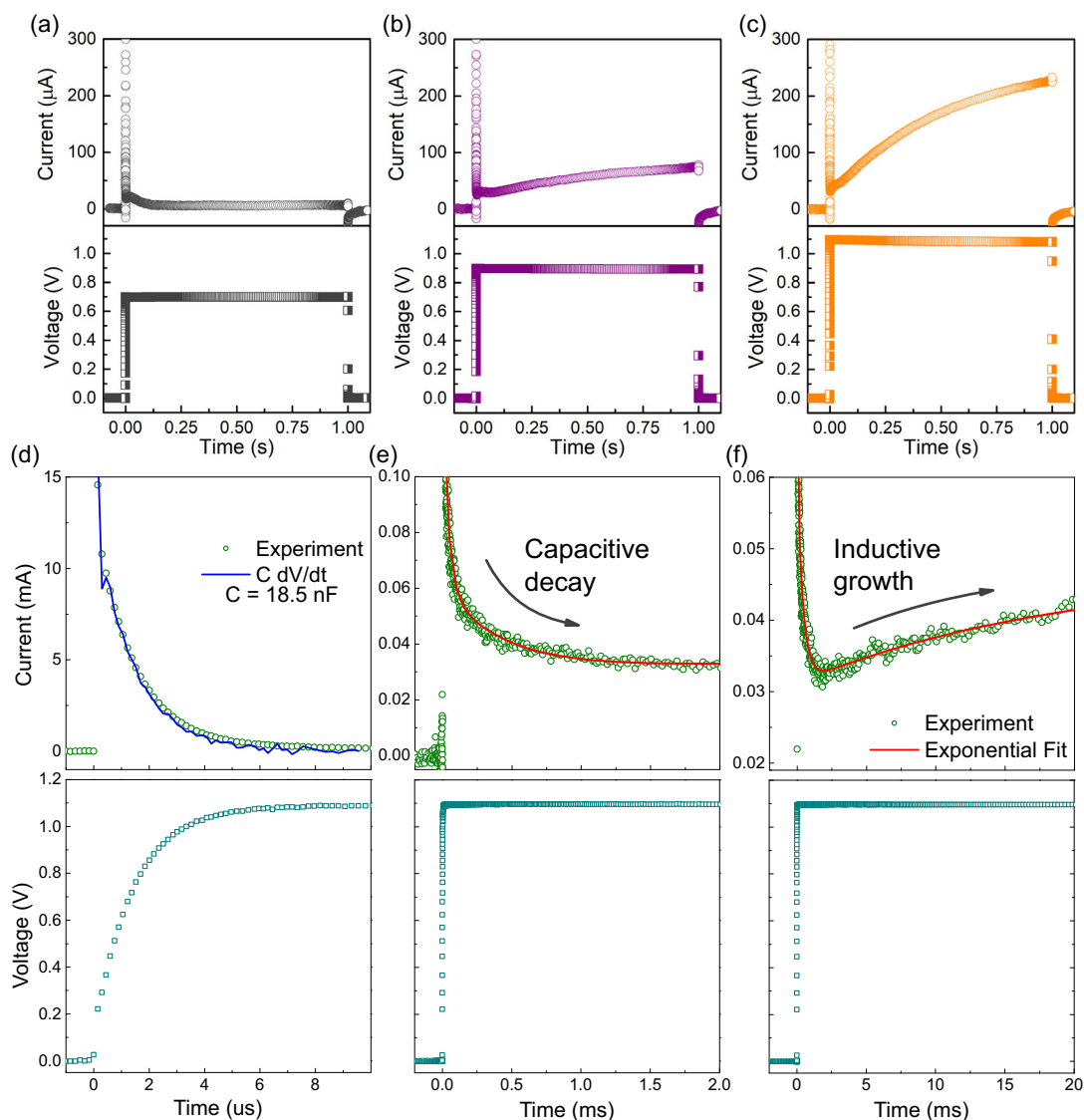
FIGURE 2 | Transient response in the dark for a PSC after a voltage pulse of (a) 0.7 V, (b) 0.9 V, and (c) 1.1 V. The transient of the 1.1 V pulse is shown for three different time scales: (d) 10 us, (e) 2 ms, and (f) 20 ms. The solid blue line in plot (d) represents the current simulation from $C\mathrm{d}V/\mathrm{d}t$, considering a capacitance of 18.5 nF, while the red lines in plots (e) and (f) are related to an exponential fitting.

between two quasiequilibrium states that are shaped by the system's prior exposure to light, voltage, or thermal history. As such, a decaying current might reflect trap-assisted relaxation in one context, but ionic screening dynamics or delayed charge activation in another. As explored in the next section, our modeling framework accommodates this complexity by allowing for multiple memory processes, each governed by its own time constant and activation function, without enforcing a direct one-to-one mapping between transient direction and process type. Accordingly, the labels 'capacitive decay' and 'inductive growth' used in panels 2(e) and 2(f), respectively, do not stem from the transient shapes alone, but are inferred based on their correspondence with the spectral features shown in Figure 3e–g. Only through the frequency-domain analysis, such as the sign of the susceptance or the presence of a low-frequency inductive loop, can these dynamic components be reliably classified.

By applying large-signal voltage pulses in the dark, we can decompose the external current into its internal components

and directly visualize nonlinear instabilities and their characteristic timescales. This approach reveals enhanced ionic migration, field screening, and interfacial redistribution processes that remain obscured under small-signal perturbations around the Voc domain. Such decomposition not only provides a first indication of the relevant nonlinear mechanisms but also guides the selection of potential amplitudes and frequency windows for subsequent sinusoidal experiments.

The use of sinusoidal excitation as a characterization protocol was anticipated in our previous theoretical work [33]. In parallel, Bisquert et al. experimentally confirmed its value as a powerful tool for PSC analysis [39]. Building on this foundation, the present study applies the protocol under dark conditions and with voltage amplitudes larger than those typically employed in IS. These amplitudes are compatible with the triangular voltage profiles of conventional JV scans. The nonlinear regime then enables a Fourier-based analysis, linking amplitude and phase differences across frequencies to reveal dynamic hysteresis-related processes.
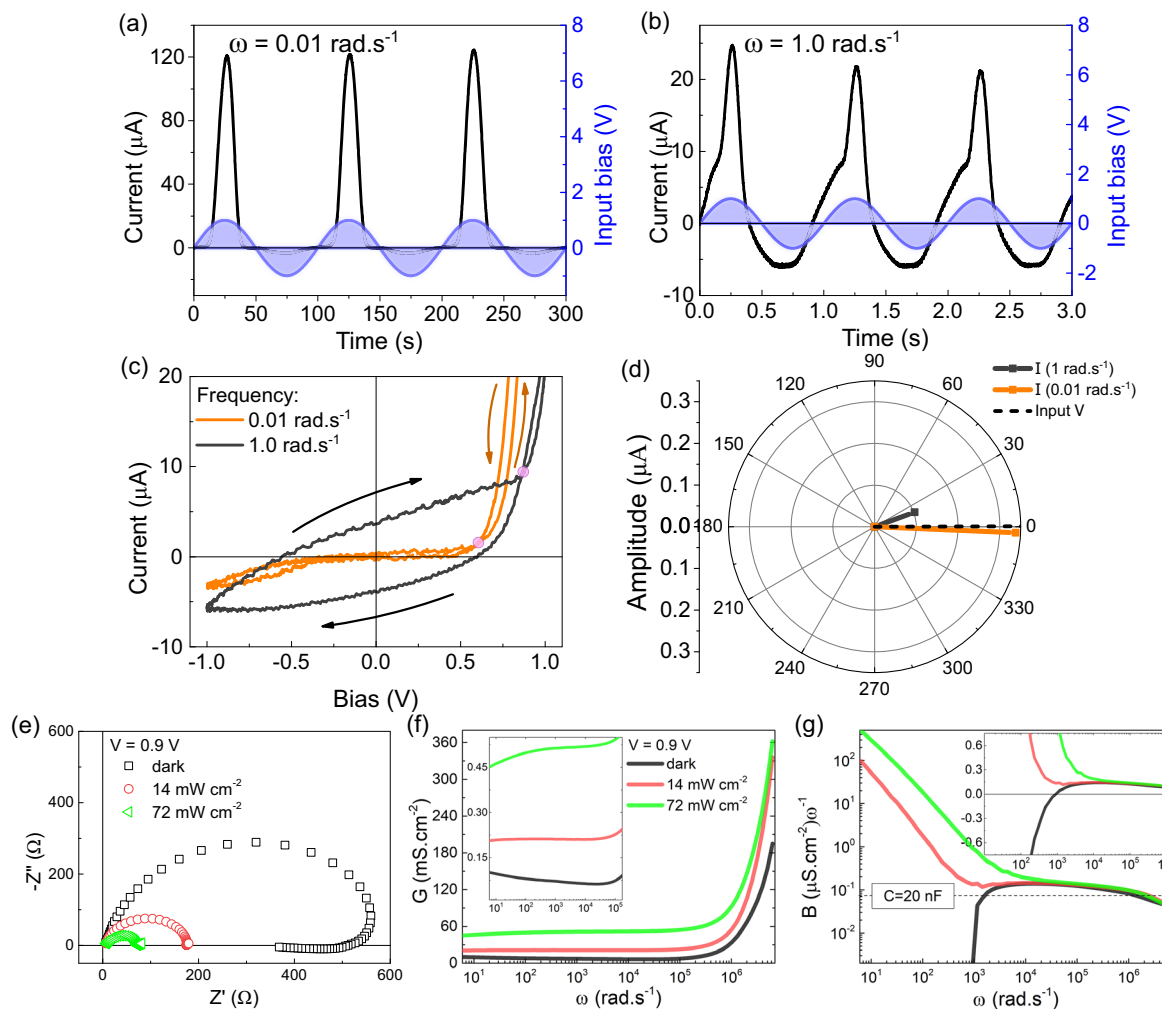
FIGURE 3 | Experimental current response in the dark under a sinusoidal voltage of 1 V applied to the PSC with (a) 0.01 rad s^{-1} and (b) 1 rad s^{-1}. (c) Current–voltage characteristics for the two frequencies. The arrows indicate the scan direction, while the pink circles highlight the transition from a capacitive (clockwise) to an inductive-like response (counterclockwise). (d) The polar map extracted from the FFT represents the capacitive and inductive-like response on the current phase compared to the input voltage. (e) Nyquist plot of the PSC with 0.9 V bias, in the dark and under illumination. IS data converted to (f) conductance and (g) susceptance plots.

From the dark transient response, our focus is on the current response at voltage biases around 1V and processes occurring on milliseconds. Figure 3 displays the steady-state current–voltage characteristics in the dark, measured using a sinusoidal voltage input of 1 V at two distinct frequencies: 0.01 and 1 rad s^{-1}, Figure 3a,b. The Sinus-J–V measurement analysis is detailed in Figure 3c. In this figure, a frequency-dependent hysteresis effect is visible. Depending on the voltammetry and IS data, hysteresis could usually be classified as capacitive or inductive. For instance, the counterclockwise hysteresis and the low-frequency loop at the Nyquist plot are both indicative of an inductive-like response [15]. In previous work [33], we observed that the frequency tuning of clockwise and counterclockwise current–voltage loops results from combinations of nonequilibrium carrier trapping and generation, respectively. These responses can be described as capacitive or inductive based on the apparent anticipation or delay of the current with respect to the voltage sweep. Therefore, the low-frequency curve in Figure 3 has an inductive-like response attributed to nonequilibrium charges, coexisting with a capacitive transport component that is

delimited by a transition point [30]. At higher frequencies, the influence of nonequilibrium charges weakens and the capacitive response dominates. As marked by the pink circles in Figure 3c, the transition points also depend on the frequency, being at 0.61 V and 0.87 V for the low and high frequency curves, respectively.

The relationship between frequency (f) and scan rate (ν) can be approximated as $f = \frac{\nu}{2\Delta E}$ [40]. The frequencies of 0.01 and 1 rad s^{-1} correspond to a triangular wave with scan rates of 40 mV s^{-1} and 4 V s^{-1}, respectively. This trend aligns with the observations by Thiesbrummel et al. [41], who reported a similar frequency-dependent hysteresis effect between 0.1 and 100 V s^{-1}. Thus, hysteresis is minimal at slower scan rates (low frequency) and becomes more pronounced at higher scan rates. At further higher scan rates, it would be expected that the ion-freeze effect mitigates hysteresis because ions cannot respond to rapid perturbations.

The map of polar coordinates in Figure 3d shows how the phase shift between voltage and current aligns with the capacitive and

inductive hysteresis response observed in Figure 3c. The plot was obtained by using the Fast Fourier transform (FFT) to convert the time-resolved sinusoidal data to the frequency domain, in which the current amplitude is related to the first harmonic of Figure S4, Supporting Information. The dashed line marks the input voltage phase, arbitrarily positioned at 0°. The excitation frequency significantly influences the current phase. At 1 rad s^{-1}, the current phase is 20°, while at 0.01 rad s^{-1} the phase is shifted to −2.4°. Fig. S6e presents the map that highlights the range of 330° to 30°. This phase analysis supports the conclusion that the dark transients exhibit inductive-like responses at slower timescales and capacitive responses at faster timescales, as demonstrated in Figure 2.

IS is commonly used in PSCs, often complemented by equivalent circuit models. These models represent the dominant components of the system, such as resistors, capacitors, and inductors, along with their interconnection. Figure 1e illustrates the IS measurements performed at 0.9 V, close to the open-circuit condition. We provide Nyquist plots to confirm that inductive loops consistently emerge when the applied bias exceeds the built-in potential (Figure S2c,d, Supporting Information). For clarity and conciseness, Figure 1e presents only three representative illumination conditions in the Nyquist plot figure: dark, 14 and 72 mW cm^{-2}. The dark measurement reveals a low-frequency loop, consistent with previous reports of a pseudo-inductive response [30]. IS data can also be analyzed using Bode plots, where the focus is on frequency response. In Figure 1f,g, we show the spectral analysis of conductance and susceptance derived from the IS data. The conductance increases proportionally with illumination intensity, while in the dark, it increases as the frequency decreases. To better observe the high-frequency response, the susceptance is plotted as B/ω, revealing its asymptotic trend toward the geometric capacitance [33]. Notably, the susceptance in the dark is negative at low frequencies, or pseudo-inductive, consistent with the loop in the Nyquist plot [42]. The conventional approach to analyze IS data involves fitting the Nyquist plot with an equivalent circuit model and interpreting the physical significance of each circuit element. Yet, it has been reported that equivalent circuit representations may not adequately capture the dynamic of nonlinear systems exhibiting inherent memory effects [36]. In summary, our contribution integrates within a single framework the key features addressed in recent works using sinusoidal perturbations [39] and transient analysis [43]. Distinctively, our methodology can combine both tools and connect them to IS through a unified analytical model validated here by experimental investigation. Therefore, in the next section, insights based on analytical modeling are presented.

2.3 | Theoretical Insights on the Charge Transport

In our previous work [33], we proposed that a multimodal framework might be better suited for a comprehensive spectral analysis as it captures the system's complexity more effectively. However, in this study, we focus on the fundamental mode ($m = 1$), commonly used in traditional IS analysis, particularly for the j_D term in Equation (1) . This approach allows for a straightforward comparison between the models.

The modular nature of our model, comprising a diode component (J_D), a photogenerated current source (J_L), multiple drift processes (J_{Mi}), and a capacitor (C), makes it broadly applicable to other optoelectronic and memory-type devices beyond PSCs. Each element corresponds directly or indirectly to a physical process: recombination, carrier generation, field-driven transport (including slow ionic motion), and dielectric response. By adjusting the weighting, activation thresholds, and timescales of these components, the same framework can be adapted to describe dynamic responses in memristors, light-emitting diodes, and other mixed ionic-electronic conductors, offering a unified approach to systems exhibiting hysteresis, memory, or frequency-dependent effects.

To accurately represent the complexity of the system, we accounted for multiple concurrent drift processes, each with distinct characteristics, such as varying relaxation times and non-equilibrium carrier transfer dynamics. Under dark conditions, the experimental data were modeled using three distinct memristive processes.

The results from the simulated IS, incorporating contributions from these memristive components, are illustrated in Figure 4. Figure 4a,b displays the Bode plots for conductance and susceptance, respectively, under dark conditions at constant voltage. These plots reveal the individual and combined responses of each memristive process. Figure 4c represents the corresponding Nyquist plot for the combined process conditions under a fixed DC bias in the dark.

At low frequencies, the experimental trends—namely, the rise in conductance and the negative susceptance observed in Figure 1f,g—were successfully reproduced by tuning the parameters in Equation (5), specifically setting $\eta < 0$ and $\alpha = 0.9$. As demonstrated in our earlier work [33], the negative susceptance originates from the reactive contribution of the system. The slight asymmetry introduced by $\alpha = 0.9$ causes the sign of the generation function to depend on the polarity of the applied bias. Expanded expressions for these terms are detailed in ref. [33].

Our model naturally captures the observed transition from capacitive to inductive response, as illustrated in Figure 4. By modeling the system with memristive components, we provide a more physically meaningful interpretation of the IS data without invoking inductive elements, which often lack physical justification in the context of solar cells.

Unlike standard equivalent circuit models, which often rely on empirical elements such as constant phase components, idealized RC networks, or fitting-dependent inductive loops, our approach is rooted in the analytical decomposition of the time-dependent drift-diffusion equations. Each component in our model corresponds to meaningful physical transport or storage mechanisms. In particular, we show that the bias and illumination-dependent modulation of the impedance response can be quantitatively described by variations in the activation and strength of specific processes, such as ion-mediated drift processes or optically enhanced carrier generation. These effects emerge from microscopic phenomena intrinsic to the hybrid perovskite system, including ionic mobility, interfacial field screening, and capacitive charging at contacts. As such, the equivalent circuit in our formulation, shown in Figure 4, is not an ad hoc construct devised to fit data but rather a compact representation of
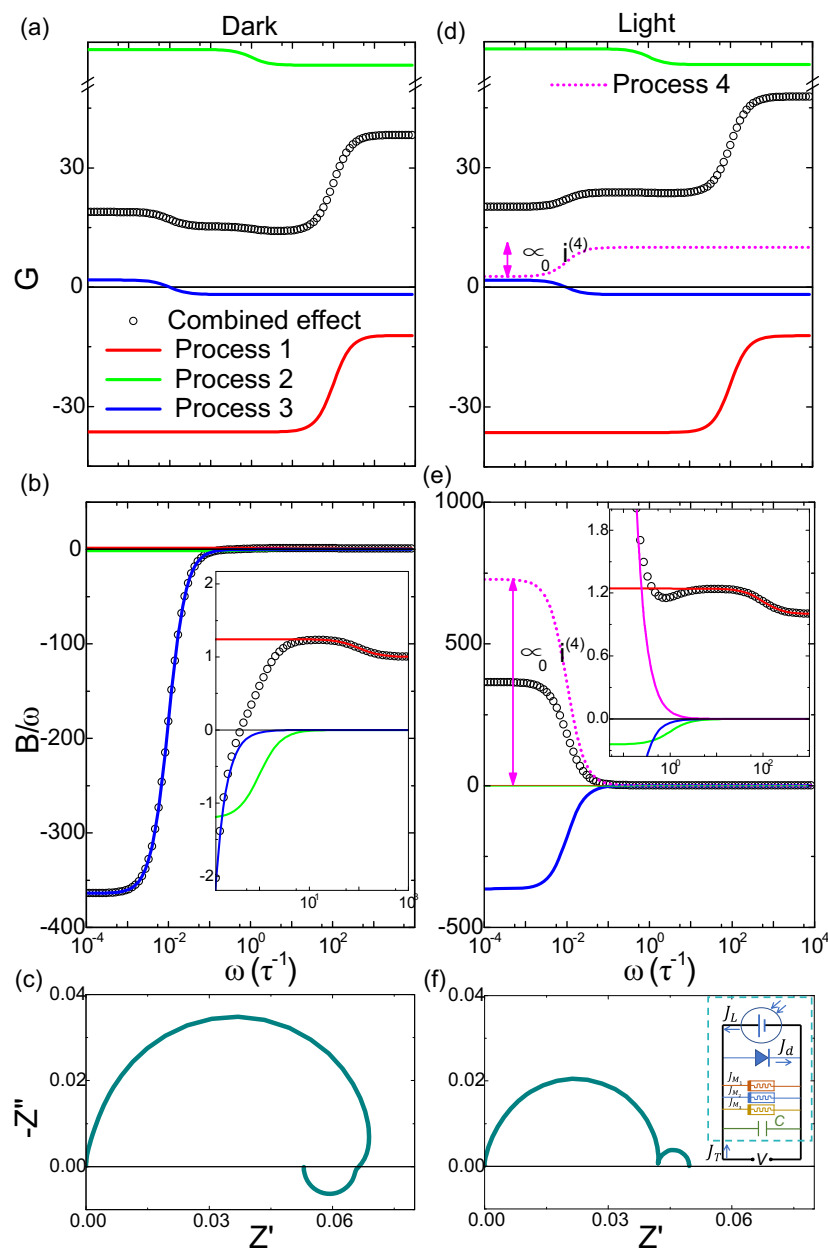
FIGURE 4 | Simulated spectra in the dark and under illumination at a fixed DC voltage. (a,d) conductance, (b,e) susceptance, and (c,f) the corresponding Nyquist maps. The inset of (f) presents the circuit from Equation (1) .

well-defined dynamical contributions, enabling predictive modeling across frequency and time domains without relying on fitting heuristics. This perspective offers a conceptual advance over conventional models linking macroscopic response directly to the underlying physics of the devices.

This model effectively captures the influence of illumination on the impedance response of the solar cell, particularly its impact on the reactive components [33]. Illumination modifies the dynamic response by altering the effective barrier heights of the memristive processes. This effect is illustrated in Figure 4d–f, where the Bode and Nyquist plots depict the impedance response with the addition of a fourth process to simulate the experimental data under illumination, as represented by the circuit diagram shown in Figure 4f and governed by Equation (1) .

Under illumination, the additional process dominates the low-frequency region and is associated with photogenerated charge carriers. This results in notable effects: a decrease in conductance, a shift to positive susceptance, and the appearance of a second semicircle in the Nyquist plot. These effects reflect altered charge dynamics introduced by the photogenerated carriers.

To strengthen the comparison between simulation and experiment, we emphasize that the observed spectral dependencies, particularly the low-frequency inductive loops in the dark and their suppression under illumination, are not only qualitatively reproduced by our model but also stem from well-defined physical mechanisms. Building on our prior analysis of nonlinear memristive systems with concurrent carrier generation and trapping processes [33, 36], we interpret these effects as signatures of delayed carrier activation and field-dependent ionic-electronic
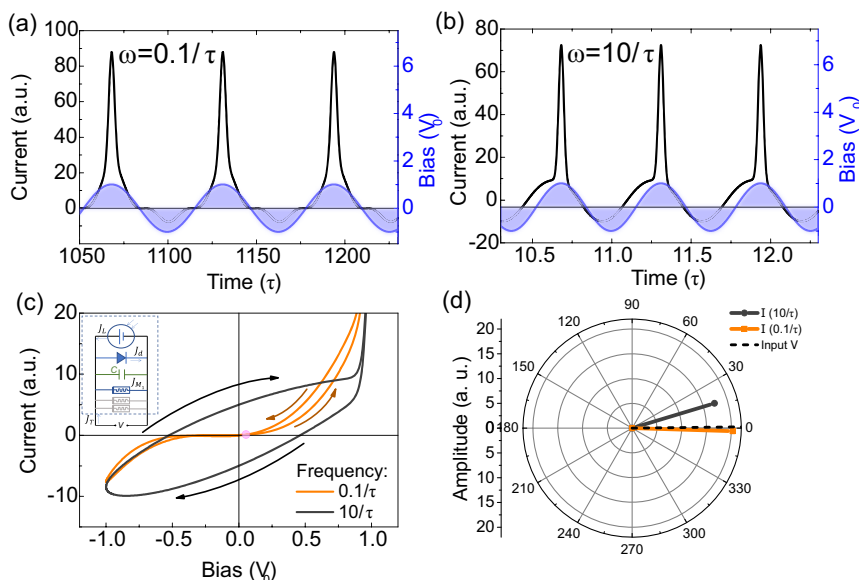
FIGURE 5 | Simulated current response in the dark under an applied sinusoidal voltage of 1 V with (a) $0.1/\tau$ and (b) $10/\tau$. (c) Current–voltage characteristic for the two frequencies. The arrows indicate the scan direction, while the pink circle highlights the transition from a capacitive (clockwise) to an inductive-like response (counterclockwise). (d) The polar map extracted from the FFT represents the capacitive and inductive-like response on the current phase compared to the input voltage. Inset in (c) is the circuit diagram of Equation (1) .

coupling. The addition of an optically responsive drift process in the illuminated condition captures the transition to a more capacitive regime, consistent with the experimental susceptance and Nyquist plots. This correspondence supports the broader relevance of our analytical framework, which connects macroscopic impedance responses to microscopic transport dynamics without relying on ad hoc circuit elements.

While the present model is not strictly quantitative, it successfully predicts the qualitative trends in the electrical response of PSCs. Furthermore, this framework offers flexibility for analyzing the system response under other experimental conditions, such as the electrical response to pulsed inputs or purely AC voltage excitations. Extending beyond traditional IS methods, this approach provides a versatile tool for examining additional PSC dynamics.

Our model, considering only the fundamental harmonic and a single drift process, is represented by the circuit diagram shown in the inset of Figure 5c. The simulated curves assume a scenario where a stationary DC voltage is superimposed on an AC voltage component. Figure 5a,b shows the current response for two AC voltage conditions. The Sinus-J–V analysis and the polar coordinate map in Figure 5c,d closely match the experimental data, validating the direct comparison between model and experiments. At higher frequency, the current exhibits a phase of 16.8°, while at lower frequency the phase shifted to −1.7°. The requirement for only one drift process suggests that the lag in output current under faster perturbations corresponds to a dominant process with a characteristic response time. The simulated curves also show the transition point for the slower sweep, highlighting the inductive-like character at such a condition, alternatively visualized by the polar map of Figure 5d. Therefore, our model successfully simulates the transition from capacitive to inductive-like without using equivalent circuits with inductive elements.

Instead, the simple analytical approach is based purely on charge trapping and generation. Additional details, including Fourier transform outputs for experimental and simulated data, are provided in the SI.

In the following work, we will analyze the sinus-J–V and FFT under illumination, which will enable better comparison to realistic solar cell measurement protocols. The advantage of using sinus-J–V is that capacitive hysteresis manifests itself as an oval-shaped current–voltage curve. The large widening corresponds to the characteristic response time of the dominant charge transport mechanism or species related to trapping phenomena. In contrast, the inductive-like response manifests by changing the loop direction above a specific transition point (Figure S6, Supporting Information). The polar map phase-magnitude representation derived from the Fourier transform provides a direct insight into the memory state of the system. In particular, the phase lag evolution under sinusoidal excitation reflects the frequency-dependent activation of transport processes modeled in our analytical framework.

In our case, the characteristic response time for the charge generation is from tens of milliseconds to seconds, supporting ion migration as the primary non-electronic cause of hysteresis. This is consistent with the mesoporous architecture and perovskite composition, since the iodide ions are relatively small compared to the lattice structure and require less activation energy for migration compared to other intrinsic ions such as Cs^+, FA^+, or Br^- [44]. Although the exact migrating species remains debated [45–47], current understanding suggests that these ions reduce charge collection efficiency by screening the internal electric field [41]. Therefore, sinus-J–V combined with the proposed analytical model is particularly helpful as it captures the frequency-dependent dynamics of ionic migration more accurately than triangular voltage sweeps and offers deeper insights

into the nonlinear process beyond the limitations of the conventional small-signal IS method.

2.4 | Practical Guidelines

In this section, a step-by-step procedure is outlined for experimentalists to extract dynamic transport parameters using transient and spectral analysis. The proposed protocol is complementary to IS and grounded in our analytical model [33] and could be summarized as:

1. Preparation and Stabilization:
   a. Prior to measurement, perform light or voltage preconditioning to reach a quasisteady state and mitigate persistent transients.

2. Voltage Pulse Transient Analysis:
   a. Apply square voltage pulses (e.g., $0 \rightarrow V_{bias}$) in the dark.
   b. Monitor current response over multiple timescales (μs to seconds).
   c. Identify and decompose the current response into: Initial capacitive spike (charging), Intermediate decay (electronic recombination or dielectric relaxation), Long-term current evolution (ion migration, polarization effects).

3. Sinusoidal Voltage Response (Sinus-J-V):
   a. Apply AC sinusoidal voltage inputs at various frequencies (e.g., 1 Hz–1 kHz), with and without illumination.
   b. Measure and analyze the phase and amplitude of the current response using the Fourier transform.
   c. Extract harmonic components and phase lags to infer memory effects, dielectric characteristic, and ion-electron coupling.

4. IS:
   a. Record impedance spectra under varying DC bias and illumination intensities across a wide frequency range (e.g., 1 MHz–1 Hz).
   b. Note deviations from typical semicircle responses (e.g., inductive loops) and their dependence on bias or light intensity.
   c. Interpret spectra qualitatively using the multi-process circuit model (Section 3): identify frequency domains linked to capacitive response (C), diode-like recombination (J_D), light-induced current (J_L), and slower ionic/migratory contributions ($J_M i$).

5. Comparison Across Conditions:

   a. Repeat measurements under different temperatures, light intensities, and aging conditions to isolate and validate each dynamic transport contribution (not presented in this work).
   b. Map experimental features onto the model described in your manuscript.
   c. Avoid purely numerical fitting with equivalent circuit schemes; instead, relate the emergence or modulation of each component to physical processes and their timescales.

   d. Use changes in transient and frequency response to track evolution in ionic mobility, trap states, or interfacial barriers
   e. Cross-check interpretations with structural, optical, or morphological data if available.

3 | Conclusion

In this work, we presented a unified analytical framework for characterizing charge transport and hysteresis in PSCs, validated through experiments on standard n-i-p mesoporous devices. By incorporating multiple voltage-activated transport processes with distinct relaxation dynamics, the model successfully reproduces the impedance spectra and transient responses without relying on conventional, empirically fitted equivalent circuits. In the dark, three independent memristive processes were sufficient to simulate the impedance response; under illumination, a fourth process was introduced to capture the enhanced carrier dynamics, matching experimental trends. Beyond small-signal IS, we demonstrated that the model also explains large-signal excitation under pulsed and sinusoidal voltage inputs. The transient response to voltage steps revealed at least three distinct dynamic regimes, linked to fast capacitive displacement, intermediate trapping effects, and slow ionic or interfacial rearrangements. Additionally, sinusoidal analysis combined with the Fourier transform revealed the system's transition from capacitive to inductive-like response, depending on excitation frequency. These observations were accurately reproduced by the model, confirming its predictive capacity across different measurement modalities. Importantly, this work provides not only theoretical insights but also practical tools. We propose a step-by-step methodology, detailed in a dedicated 'Practical Guidelines' section, that experimentalists can use to extract dynamic transport signatures and hysteresis characteristics from PSCs. This includes preconditioning protocols, selection of frequency ranges, and interpretation of amplitude/phase data using sinusoidal inputs. As such, our approach offers the photovoltaic community a physically grounded and experimentally accessible strategy for decoding and managing nonlinear and memory-driven effects in PSCs, advancing both fundamental understanding and applied device characterization.

4 | Experimental

4.1 | Experimental Details

Fluorine-doped Tin Oxide (FTO) coated glass substrates ($7\Omega \, sq^{-1}$, Sigma Aldrich) were patterned and sequentially cleaned. After drying with N_2, they were treated with UV-Ozone (Ossila Ltda) for 15 min to ensure optimal surface cleanliness. A compact Nb_2O_5 layer was deposited via reactive magnetron sputtering in a Kurt J. Lesker System. The deposition was conducted at 500°C with 240 W plasma power. The chamber was maintained at a pressure of 5.0×10^{-3} Torr, with a 40 sccm flow of high-purity argon and 3.5 sccm of oxygen. A mesoporous TiO_2 solution (150 mg/mL in ethanol) was spin-coated on top of the Nb_2O_5 compact layer. Both compact and mesoporous layers were annealed at 550 C for 60 min. FTO/Nb_2O_5/TiO_2 substrates were transferred to a nitrogen-filled glovebox for device fabrication. A $Cs_{0.17}FA_{0.83}Pb(I_{0.83}Br_{0.17})_3$ double-cation mixed-halide

perovskite solution was prepared by combining two separately prepared solutions: one iodide-based (1.2 M PbI_2, 1.0 M FAI, 0.2 M CsI in DMF:DMSO, 4:1 v/v) and one bromide-based (1.2 M $PbBr_2$, 1.2 M FABr in DMF:DMSO, 4:1 v/v). The perovskite film was deposited via spin-coating: first at 1000 rpm for 10 s, then at 6000 rpm for 25 s, with 200 μL of chlorobenzene (anti-solvent) dropped after 20 s. The perovskite film was first annealed at 60°C for 3 min and then at 120°C for 30 min to promote crystallization. The hole transporting layer was based on Spiro-OMeTAD (73 mg/mL in chlorobenzene) doped with 29 μL of 4-tert-butyl pyridine, 29 μL of FK209 cobalt complex solution (300 mg/mL in acetonitrile), and 18 μL of lithium bis (trifluoromethanesulfonic)imide (Li-TFSI) solution (520 mg/mL in acetonitrile). Finally, an 80 nm gold electrode was thermally evaporated onto the device integrated into the Glove Box. More details on the depositions can also be found in the previous publication [20, 21].

J–V curves were measured using a Keithley 2400 source measurement unit under simulated sunlight (AM 1.5G,100mWcm^{-2}) from a Newport Class AAA solar simulator (model 94023AU), calibrated with a certified silicon solar cell. EQE measurements were carried out with a PTS-3-PTD photothermal deflection system from ScienceTech. Additional electrical characterization was performed using the PAIOS system (Fluxim AG). The techniques included staircase sweep J–V, where data points are acquired step-by-step for higher precision, dark injection transients, which apply a voltage step and measure the resulting transient current, and Sinus-J-V measurements by a sinusoidal voltage input and plotting the resulting current versus voltage. IS involves applying a small AC signal (50 mV) superimposed on a DC bias and measuring current across a range of frequencies.

4.2 | Analytical Model

The analytical model employed in this study builds on our previous work [33]. In summary, for an arbitrary bias voltage, V, the total current density, j_T, is decomposed into three independent components,

$$j_T = j_D + \frac{C_g}{A}\frac{dV}{dt} + \sum_i j_{M_i} \quad (1)$$

where j_D represents the diode current density. This term represents the current derived from minority carrier diffusion at the boundaries of the depletion (or intrinsic) region

$$j_D = eD_n \frac{\partial n}{\partial z}\Big|_{z=-\frac{\Delta}{2}} - eD_p \frac{\partial p}{\partial z}\Big|_{z=\frac{\Delta}{2}} \quad (2)$$

of width Δ. The axis origin is set at the mid-point of the depletion region, assuming uniform electron and hole current components [48].

The second term in Equation (1) describes the displacement current contribution due to the geometric capacitance, C_g, of the device with area A. The third term models memory-related contributions, including ionic processes, fluctuations, and potential leakage pathways (labeled with the sub-index i). It is expressed as,

$$j_{M_i} = \gamma_i (N_i^0 + \delta N_i)V \quad (3)$$

where $\gamma_i = \frac{e\mu_i}{A\Delta^2}$ is the ionic mobility term along Δ, and $N_i^0 + \delta N_i$ represents the fluctuating nonequilibrium carrier population around N_i^0 with a relaxation time τ_i [49, 50],

$$\frac{d\delta N_i}{dt} = -\frac{\delta N_i}{\tau_i} + g_i(V). \quad (4)$$

According to Silva et al. [49], the carrier generation or trapping rate is described by a transfer function

$$g(V) = \frac{i_0}{\eta}\left[e^{-\eta_L \frac{eV}{k_B T}} + e^{\eta_R \frac{eV}{k_B T}} - 2\right] \quad (5)$$

where $i_0 = \frac{4\pi m^* A}{(2\pi\hbar)^3}(k_B T)^2 e^{-\frac{E_B}{k_B T}}$, $\eta_L = \alpha\eta/(1+\alpha)$, and $\eta_R = \eta/(1+\alpha)$. Here, $\alpha \in [0, \infty)$ characterizes the symmetry of the carrier transfer with respect to the local bias voltage drop. The case $\alpha = 1$ corresponds to symmetric transfer, while $\eta > 0$ and $\eta < 0$ represent pure generation and pure trapping scenarios, respectively. The terms j_D and j_{M_i} from Equation (1) were thoroughly expanded in ref. [50].

For this study, both AC and DC conditions are addressed using the general voltage expression $V = V_S + V_0 \cos(\omega t)$, encompassing cyclic voltammetry and IS characterizations for arbitrary V_S. The combination of these terms consistently reproduces memory effects [13, 49, 50], providing a framework to correlate current–voltage characteristics with IS measurements.

Conflicts of Interest

The authors declare no conflicts of interest.

Data Availability Statement

The data that support the findings of this study are available from the corresponding author upon reasonable request.

References

1. M. Noman, Z. Khan, and S. T. Jan, "A Comprehensive Review on the Advancements and Challenges in Perovskite Solar Cell Technology," *RSC Advances* 14 (2024): 5085–5131.

2. G. Koutsourakis, C. Worsley, and M. Spence, "Investigating Spatial Macroscopic Metastability of Perovskite Solar Cells with Voltage Dependent Photoluminescence Imaging," *Journal of Physics: Energy* 5 (2023): 025008.

3. E. Ghahremanirad, O. Almora, S. Suresh, A. A. Drew, T. H. Chowdhury, and A. R. Uhl, "Beyond Protocols: Understanding the Electrical Behavior of Perovskite Solar Cells by Impedance Spectroscopy," *Advanced Energy Materials* 13 (2023): 2204370.

4. J. A. Anta, G. Oskam, and P. Pistor, "The Dual Nature of Metal Halide Perovskites," *The Journal of Chemical Physics* 160 (2024): 150901. https://doi.org/10.1063/5.0190890.

5. W. Tress, N. Marinova, T. Moehl, S. M. Zakeeruddin, M. K. Nazeeruddin, and M. Grätzel, "Understanding the Rate-Dependent j–v Hysteresis, Slow Time Component, and Aging in ch 3 nh 3 pbi 3 Perovskite Solar Cells: The Role of a Compensated Electric Field," *Energy & Environmental Science* 8 (2015): 995–1004.

6. J. Bisquert, "Hysteresis, Impedance, and Transients Effects in Halide Perovskite Solar Cells and Memory Devices Analysis by Neuron-Style Models," *Advanced Energy Materials* 14 (2024): 2400442.

7. A. Guerrero, J. Bisquert, and G. Garcia-Belmonte, "Impedance Spectroscopy of Metal Halide Perovskite Solar Cells from the Perspective of Equivalent Circuits," *Chemical Reviews* 121 (2021): 14430–14484.

8. J. Bisquert, A. Guerrero, and C. Gonzales, "Theory of Hysteresis in Halide Perovskites by Integration of the Equivalent Circuit," *ACS Physical Chemistry Au* 1 (2021): 25–44.

9. S. Liu, J. Zeng, Q. Chen, and G. Liu, "Recent Advances in Halide Perovskite Memristors: From Materials to Applications," *Frontiers of Physics* 19 (2024): 23501.

10. J. Bisquert, "Current-Controlled Memristors: Resistive Switching Systems with Negative Capacitance and Inverted Hysteresis," *Physical Review Applied* 20 (2023): 044022, https://doi.org/10.1103/PhysRevApplied.20.044022.

11. J. Bisquert, A. Bou, A. Guerrero, and E. Hernández-Balaguera, "Resistance Transient Dynamics in Switchable Perovskite Memristors," *APL Machine Learning* 1 (2023): 036101, https://doi.org/10.1063/5.0153289.

12. L. Chua, "Memristor-the Missing Circuit Element," *IEEE Transactions on Circuit Theory* 18 (1971): 507–519, https://doi.org/10.1109/TCT.1971.1083337.

13. V. Lopez-Richard, R. S. W. Silva, O. Lipan, and F. Hartmann, "Tuning the Conductance Topology in Solids," *Journal of Applied Physics* 133 (2023): 134901, https://doi.org/10.1063/5.0142721.

14. A. Ascoli, R. Tetzlaff, L. O. Chua, J. P. Strachan, and R. S. Williams, "History Erase Effect in a Non-Volatile Memristor," *IEEE Transactions on Circuits and Systems I: Regular Papers* 63 (2016): 389–400, https://doi.org/10.1109/TCSI.2016.2525043.

15. J. Bisquert, "Inductive and Capacitive Hysteresis of Current-Voltage Curves: Unified Structural Dynamics in Solar Energy Devices, Memristors, Ionic Transistors, and Bioelectronics," *PRX Energy* 3 (2024): 011001.

16. M. De Bastiani, G. Dell'Erba, and M. Gandini, "Ion Migration and the Role of Preconditioning Cycles in the Stabilization of the j-v Characteristics of Inverted Hybrid Perovskite Solar Cells," *Advanced Energy Materials* 6 (2016): 1501453.

17. J. Shao, S. Yang, L. Lei, Q. Cao, Y. Yu, and Y. Liu, "Pore Size Dependent Hysteresis Elimination in Perovskite Solar Cells Based on Highly Porous TiO$_2$ Films with Widely Tunable Pores of 15–34 nm," *Chemistry of Materials* 28 (2016): 7134–7144.

18. W. Clarke, G. Richardson, and P. Cameron, "Understanding the Full Zoo of Perovskite Solar Cell Impedance Spectra with the Standard Drift-Diffusion Model," *Advanced Energy Materials* 14 (2024): 2400955.

19. Agustin O. Alvarez, S. Ravishankar, and F. Fabregat-Santiago, "Combining Modulated Techniques for the Analysis of Photosensitive Devices," *Small Methods* 5 (2021): 2100661.

20. H. G. Lemos, J. H. Rossato, and R. A. Ramos, "Electron Transport Bilayer with Cascade Energy Alignment Based on Nb$_2$O$_5$–Ti$_3$C$_2$ MXene/TiO$_2$ for Efficient Perovskite Solar Cells, "*Journal of Materials Chemistry C* 11 (2023): 3571–3580.

21. S. L. Fernandes, L. D. O. Garcia, R. D. A. R. Júnior, et al., "The Role of Nb$_2$O$_5$ Deposition Process on Perovskite Solar Cells," *Journal of Renewable and Sustainable Energy* 14 (2022): 043703.

22. W. Clarke, M. V. Cowley, M. J. Wolf, P. Cameron, A. Walker, and G. Richardson, "Inverted Hysteresis as a Diagnostic Tool for Perovskite Solar Cells: Insights from the Drift-Diffusion Model," *Journal of Applied Physics* 133 (2023): 095001.

23. F. Wu, R. Pathak, and K. Chen, "Inverted Current–voltage Hysteresis in Perovskite Solar Cells," *ACS Energy Letters* 3 (2018): 2457–2460.

24. E. Hernández-Balaguera and J. Bisquert, "Time Transients with Inductive Loop Traces in Metal Halide Perovskites," *Advanced Functional Materials* 34 (2024): 2308678, https://doi.org/10.1002/adfm.202308678.

25. J. P. F. Assunção, H. G. Lemos, and J. H. Rossato, "Interface Passivation with Ti$_3$C$_2$T$_X$-MXene Doped Pmma Film for Highly Efficient and Stable Inverted Perovskite Solar Cells," *Journal of Materials Chemistry C* 12 (2024): 562–574, https://doi.org/10.1039/D3TC03810F.

26. P. Calado, A. M. Telford, and D. Bryant, Evidence for Ion Migration in Hybrid Perovskite Solar Cells with Minimal Hysteresis," *Nature Communications* 7 (2016): 13831.

27. W. Tress, "Metal Halide Perovskites as Mixed Electronic-Ionic Conductors: Challenges and Opportunities-from Hysteresis to Memristivity," *The Journal of Physical Chemistry Letters* 8 (2017): 3106–3114.

28. S. A. Weber, I. M. Hermes, and S. H. Turren-Cruz, "How the Formation of Interfacial Charge Causes Hysteresis in Perovskite Solar Cells, "*Energy & Environmental Science* 11 (2018): 2404–2413.

29. O. J. Sandberg, J. Kurpiers, and M. Stolterfoht, "On the Question of the Need for a Built-in Potential in Perovskite Solar Cells," *Advanced Materials Interfaces* 7 (2020): 2000041.

30. C. Gonzales, A. Guerrero, and J. Bisquert, "Transition from Capacitive to Inductive Hysteresis: A Neuron-Style Model to Correlate i–v Curves to Impedances of Metal Halide Perovskites," *The Journal of Physical Chemistry C* 126 (2022): 13560–13578.

31. E. Hernández-Balaguera and J. Bisquert, "Accelerating the Assessment of Hysteresis in Perovskite Solar Cells," *ACS Energy Letters* 9 (2024): 478–486.

32. E. Hernández-Balaguera and J. Bisquert, "Negative Transient Spikes in Halide Perovskites," *ACS Energy Letters* 7 (2022): 2602–2610.

33. V. Lopez-Richard, L. A. MeneghettiJr, G. L. Nogueira, F. Hartmann, and C. F. Graeff, "Unified Model for Probing Solar Cell Dynamics via Cyclic Voltammetry and Impedance Spectroscopy," *Physical Review B* 110 (2024): 115306.

34. E. Von Hauff and D. Klotz, "Impedance Spectroscopy for Perovskite Solar Cells: Characterisation, Analysis, and Diagnosis," *Journal of Materials Chemistry C* 10 (2022): 742–761.

35. S. E. O'Kane, G. Richardson, and A. Pockett, "Measurement and Modelling of Dark Current Decay Transients in Perovskite Solar Cells,"*Journal of Materials Chemistry C* 5 (2017): 452–462, https://doi.org/10.1039/C6TC04964H.

36. V. Lopez-Richard, S. Pradhan, and R. S. Wengenroth Silva, "Beyond Equivalent Circuit Representations in Nonlinear Systems with Inherent Memory," *Journal of Applied Physics* 136 (2024): 165103.

37. A. L. Costa Silva, R. Silva, and L. A. Moises, "From Memory Traces to Surface Chemistry: Decoding REDOX Reactions," *ACS Applied Electronic Materials* 7 (2025): 1439–1447.

38. V. Lopez-Richard, I. R. Filgueira e Silva, and A. Ames, The Emergence of Mem-Emitters," *Nano Letters* 25 (2024): 1816–1822.

39. E. Balaguera and J. Bisquert, "Evolution of Performance Parameters of Perovskite Solar Cells with Current–Voltage Scan Frequency," *Energy & Fuels* 39 (2025): 3638–3648.

40. M. Schalenbach, Y. E. Durmus, H. Tempel, H. Kungl, and R. A. Eichel, "Double Layer Capacitances Analysed with Impedance Spectroscopy and Cyclic Voltammetry: Validity and Limits of the Constant Phase Element Parameterization," *Physical Chemistry Chemical Physics* 23 (2021): 21097–21105.

41. J. Thiesbrummel, S. Shah, and E. Gutierrez-Partida, "Ion-Induced Field Screening as a Dominant Factor in Perovskite Solar Cell Operational Stability," *Nature Energy* 9 (2024): 664.

42. J. Bisquert and A. Guerrero, "Chemical Inductor," *Journal of the American Chemical Society* 144 (2022): 5996–6009, https://doi.org/10.1021/jacs.2c00777.

43. E. Balaguera and J. Bisquert, "Mapping of Internal Ionic/Electronic Transient Dynamics in Current–Voltage Operation of Perovskite Solar Cells," *Small* 21 (2025): 2409534.

44. L. Zuo, Z. Li, and H. Chen, "Ion Migration and Accumulation in Halide Perovskite Solar Cells," *Chinese Journal of Chemistry* 41 (2023): 861–876.

45. L. Gollino, D. Zheng, N. Mercier, and T. Pauporté, Unveiling of a Puzzling Dual Ionic Migration in Lead-and Iodide-Deficient Halide Perovskites (d-Hps) and Its Impact on Solar Cell j–v Curve Hysteresis," in Exploration (Wiley Online Library, 2024), 20220156, https://doi.org/10.1002/EXP.20220156.

46. S. Yuan, F. Lou, and Y. Li, "Targeted Suppression of Hysteresis Effect in Perovskite Solar Cells through the Inhibition of Cation Migration," *Applied Physics Letters* 122 (2023): 133502, https://doi.org/10.1063/5.0145249.

47. S. Tammireddy, M. N. Lintangpradipto, and O. Telschow, "Hysteresis and Its Correlation to Ionic Defects in Perovskite Solar Cells," *The Journal of Physical Chemistry Letters* 15 (2024): 1363–1372, https://doi.org/10.1021/acs.jpclett.3c03146.

48. M. A. Green, Solar Cells: Operating Principles, Technology, and System Applications, Prentice-Hall Series in Solid State Physical Electronics (Prentice-Hall, 1982).

49. R. S. W. Silva, F. Hartmann, and V. Lopez-Richard, "The Ubiquitous Memristive Response in Solids," *IEEE Transactions on Electron Devices* 69 (2022): 5351–5356, https://doi.org/10.1109/TED.2022.3188958.

50. A. B. de Paiva, R. S. Wengenroth Silva, and M. P. F. de Godoy, "Temperature, Detriment, or Advantage for Memory Emergence: The Case of Zno," *The Journal of Chemical Physics* 157 (2022): 014704, https://doi.org/10.1063/5.0097470.

Supporting Information

Additional supporting information can be found online in the Supporting Information section. **Supporting Fig. 1**: (a) Experimental EQE and integral current density of a representative n-i-p device. (b) Normalized plots of the EQE and its derivatives, from where we extract the inflection point of $\lambda_g = 750$nm (1.653 eV) and $\lambda_s = 20$nm. (c) Sigmoid parametrization of EQE spectra, where the solid squares represent the experimental data, and the blue line is the fit to Eq. S1 in the region of the photovoltaic bandgap. **Supporting Fig. 2**: (a) current-voltage curve measured under an illumination intensity of 72 mW cm^{-2}, both before and after chronoamperometry-assisted stabilization. A pre-bias of 1V in the dark was applied as a preconditioning step between measurements. (b) Hysteresis response under illumination for a scan rate variation from 40 to 400 mV s^{-2}. Nyquist plots under varying illumination intensities in Figure (c), and in Figure (d) we show Nyquist plots recorded in the dark under different DC offset voltages. **Supporting Fig. 3**: (a) Current-voltage curves under different illumination intensity, used to calculate the ideality factor. (b) V_{oc} vs light intensity plot obtained from the current-voltage curves measured from a reverse sweep under different illumination intensities. (c) Plot of capacitance against frequency measured in the dark. **Supporting Fig. 4**: Fast Fourier Transform (FFT) algorithm applied to the experimental sinusoidal data obtained from the n-i-p mesoporous PSC using the PAIOS equipment. **Supporting Fig. 5**: Fast Fourier Transform (FFT) algorithm applied to the simulated sinusoidal data. **Supporting Fig. 6**: Plots extracted from the Sinus-J-V characterization and simulated data, both for the dark condition. Current-voltage response on the linear scale, with the arrows indicating the scan direction. The experimental data were obtained for (a) 0.01 rad.s^{-1} and (b) 1.0 rad.s^{-1}. The simulation considered the frequencies of (c) $0.1/\tau$ and (d) $10/\tau$. The transition voltage marked by the blue circle separates the capacitive and the inductive-like effects. Polar map highlighting the capacitive and inductive-like effect on the current phase compared to the input voltage, where (e) is the experimental data and (f) the simulated one. **Supporting Table 1**: Parameters used in the exponential function (Eq. S3) to fit the current decay and growth after a voltage pulse.